Plasma-enhanced pulsed-laser deposition of single-crystalline Mo_2C ultrathin superconducting films

Fan Zhang, Zhi Zhang, Huichao Wang, Cheuk Ho Chan, Ngai Yui Chan, Xin Xin Chen, and Ji-Yan Dai*
Department of Applied Physics, The Hong Kong Polytechnic University, Hong Kong, 999077, P. R. China
(Received 20 April 2017; published 21 August 2017)

Transition-metal carbides (TMCs) possess many intriguing properties and inspiring application potentials, and recently the study of a two-dimensional form of TMCs has attracted great attention. Herein, we report successful fabrication of continuous Mo_2C ultrathin single-crystalline films at 700 °C with an approach of plasma-enhanced pulsed-laser deposition. By sophisticated structural analyses, the Mo_2C films are characterized as single crystal with a rarely reported face-centered cubic structure. In further electrical transport measurements, superconductivity observed in the Mo_2C films demonstrates a typical two-dimensional feature, which is consistent with Berezinskii-Kosterlitz-Thouless transitions. Besides, large upper critical magnetic fields are discovered in this system. Our work offers an approach to grow large-area and high-quality TMCs at relatively low temperatures. This study may stimulate more related investigations on the synthesis, characterizations, and applications of two-dimensional TMCs.

DOI: 10.1103/PhysRevMaterials.1.034002

I. INTRODUCTION

In the past decade, two-dimensional (2D) materials have attracted much attention due to their unique properties, and indeed, 2D materials are good platforms to study interesting phenomena and explore potential applications in high-performance devices [1–4]. In the very large material family, most 2D materials are semiconductors or dielectrics, while the choice of metallic conductor is rare. Transition-metal carbides (TMCs) in a 2D MXenes form are recently discovered to be produced by selective etching of the A element from the $M_{n+1}AX_n$ ($n = 1$, 2, or 3) (MAX) phases, where M denotes a transition metal, A is an A-group element, and X is either carbon or nitrogen [5–7]. As newly joined members of 2D materials, TMCs usually exhibit good electrical conductivity, and even superconductivity at low temperatures [8–10]. Besides, they possess excellent mechanical properties, thermal stability, and catalytic activity comparable to noble metals, suggesting great value of applications in energy storage, catalysis, and other electronic devices [11–19].

Molybdenum carbide is a well-known TMC that has been explored for interesting physics phenomenon and application potentials due to its catalytic property and superconductivity [20–24]. A lot of works have been done to synthesize Mo_2C in different phases and scales. Orthorhombic α-Mo_2C and hcp β-Mo_2C are the two stable crystalline forms of molybdenum carbide [25]. By reactive sputtering Mo in an acetylene atmosphere, Lee *et al.* synthesized superconducting Mo-C thin film while its crystallinity remains unknown [24]. With a plasma-enhanced chemical vapor deposition (PECVD) method followed by a temperature-programmed reduction (TPR) process, phase-pure polycrystalline β-Mo_2C films were fabricated by Wolden *et al.* [26]. Very recently, Halim *et al.* realized large-scale synthesis and delamination of 2D Mo_2CT_x flakes by selectively etching Ga from Mo_2Ga_2C powders in acid solutions [27]. Mo_2C obtained in this way suffers from structural defects and impurity-terminated surfaces. In addition, the lateral dimensions of samples grown by these methods are also limited for further investigation of the intrinsic physical properties of 2D Mo_2C and constrains future large-area applications. Single-crystalline 2D Mo_2C had not been synthesized until Xu *et al.* reported the method of a modulated chemical vapor deposition (CVD) process by which high-quality 2D ultrathin α-Mo_2C superconducting crystals with maximum size over 100 μm were grown at temperatures over 1085 °C [9]. With an ambient-pressure CVD method (APCVD) at temperature above 1100 °C, Geng *et al.* found a way to control thickness and morphology of high-crystallinity Mo_2C at a nanometer scale [28]. However, the high nucleation density at high growth temperature involved in the CVD method used by Xu *et al.* and Geng *et al.* hinders the possibility to precisely control the growth of Mo_2C in thickness and area simultaneously. Much effort is still necessary to further improve the knowledge of growth methods and intrinsic properties of 2D Mo_2C.

Here, we report the growth of large-area single-crystalline Mo_2C, which is epitaxially grown by a plasma-enhanced pulsed-laser deposition (PEPLD) method. Plasma enhancement is adopted in conventional CVD systems to facilitate material synthetizations with lower temperature and higher quality [29–31]. Pulsed-laser deposition (PLD) is a traditional thin-film deposition method which renders researchers a way to grow high-quality thin films of variant materials such as oxides [32], metals [33], and even 2D materials [34–36]. Combining the advantages of PECVD and PLD, we successfully grow continuous single-crystalline Mo_2C films of different thicknesses on sapphire (0001). The growth temperature is 700 °C. The sample thickness could be controlled by the laser pulse number. The ionization of methane has the function of enhancing the reaction between molybdenum and carbon, while the existence of ionized hydrogen should be useful to maintain the Mo in a desired valence state, being free from forming Mo oxides. Such single-crystalline Mo_2C film has the largest area reported so far and possesses rarely reported fcc phase, having typical two-dimensional superconducting properties consistent with Berezinskii-Kosterlitz-Thouless (BKT) behavior. Compared to Mo_2C in other structures [9,24,28], the fcc-Mo_2C shows a similar thickness-dependent critical temperature change but a much higher upper critical field of

*jiyan.dai@polyu.edu.hk

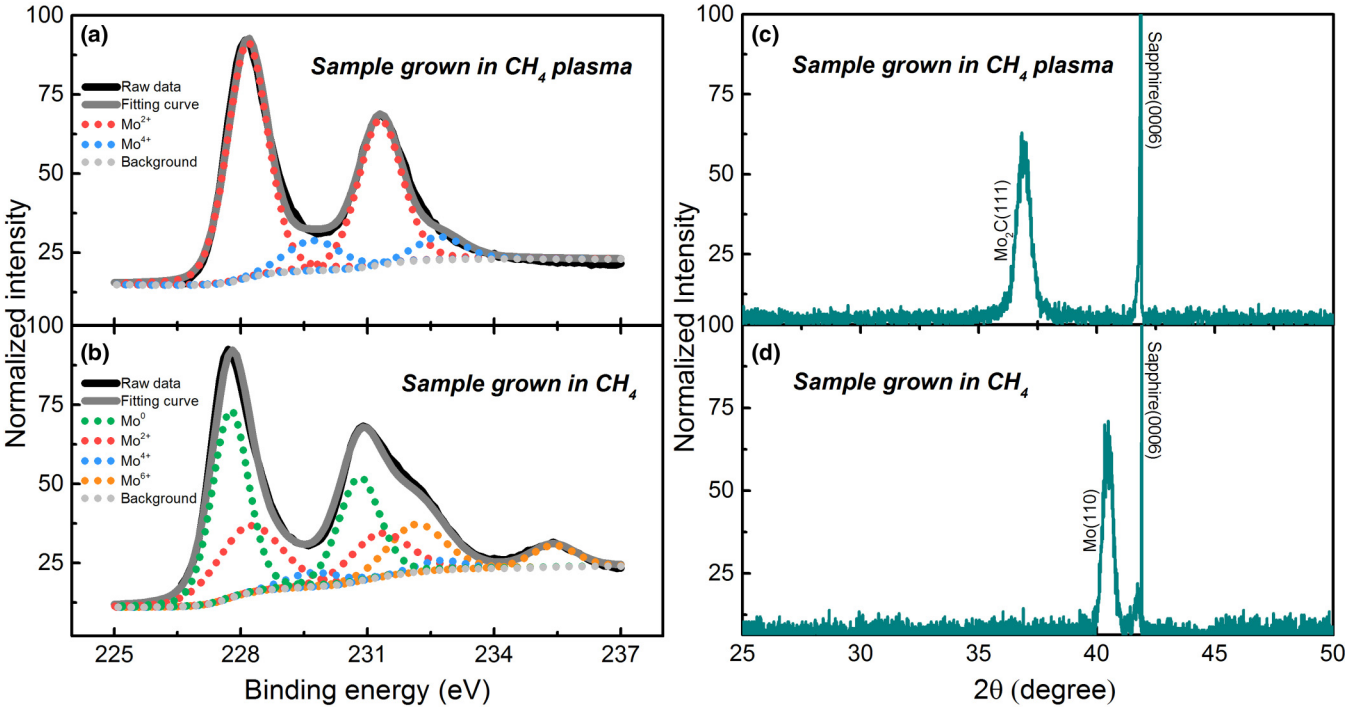

FIG. 1. Sample composition and structure analysis by XPS and XRD. Left: XPS analysis for the sample grown (a) in ionized CH_4 plasma and (b) nonionized CH_4. Right: XRD pattern for the sample grown (c) in ionized CH_4 plasma and (d) nonionized CH_4.

its superconductivity. Such a PEPLD method could also be adopted for growing other ultrathin transition-metal carbides and nitrides.

II. EXPERIMENTS

In our PEPLD system, the plasm is generated by modifying a conventional PLD system to be equipped with a high-voltage electrode at the methane inlet of the chamber which can ionize the gas when it was vented into the chamber. A dc voltage of 500 V is supplied by a power generator. Before deposition, the chamber was vented by CH_4 to a pressure of 15 Pa, and the CH_4 was ionized to generate plasma by glow discharge. A KrF laser (Lambda Physik COMPex 205) with a wavelength of 248 nm was used to focus on a Mo metal target. The energy density was set to be about 5 J mm^{-2} with a pulse frequency of 5 Hz. The sapphire (0001) substrate is adjusted to be 3.5 cm away from the target location and heated to 700 °C for film deposition. After growth, the sample was cooled down to room temperature in vacuum naturally. Transport properties can be characterized directly on the grown sample without any etching or transfer process. (A schematic illustration of the PEPLD system is provided in the Supplemental Material Fig. S1, and the appearance of the grown sample is shown in Fig. S2 [37].) The growth temperature is monitored by infrared temperature sensors (Raytek-MM2ML). Sample thicknesses ranging from 2 to 25 nm are controlled by deposition time (Supplemental Material, Table S1 [37]).

The grown Mo_2C film composition is investigated by conducting x-ray photoelectron spectroscopy (XPS) and x-ray diffraction (XRD) measurements, and the lattice structure is further confirmed by transmission electron microscopy (TEM). The XPS measurement is done by a SKL-12 spectrometer modified with a VG CLAM 4 multichannel hemispherical analyzer and equipped with Al/Mg twin anode x-ray sources. XRD and x-ray reflectivity (XRR) analysis is carried out in Rigaku SmartLab. Both the cross-sectional TEM specimens and plane-view TEM specimens were prepared first by mechanical mining followed by ion-beam thinning using a Gatan precision ion polishing system. The detailed structural characteristics of the specimens were investigated by TEM (JEOL 2100F, operated at 200 kV). Electric and magnetic properties of the films are conducted in a physical properties measurement system (Quantum Design). Aluminum wires are ultrasonically bonded on the film for electrical transportation characterization. Through the standard four-probe method, a constant current source of 0.5 μA is supplied on the film for electrical measurement.

III. RESULTS AND DISCUSSION

To confirm the film composition and chemical state of Mo atoms, XPS measurement was performed. The measured Mo 3*d* spectrum and fitting curves of samples grown in different conditions are shown in Figs. 1(a) and 1(b). It is seen that for the sample grown in CH_4 plasma, the Mo^{2+} state dominates the spectra and these Mo ions are believed to be from Mo_2C. It is noticed that there is also a small amount of Mo^{4+} which may come from defects where MoC forms. The XPS analysis results of the sample grown in nonionized CH_4 atmosphere show that the film is mainly molybdenum metal, where Mo of chemical states from +2 to +6 also exist. To investigate the crystallinity of the film, XRD characterization was carried out for both films grown in ionized or nonionized CH_4 environments. In Figs. 1(c) and 1(d), the sharp peak at 41.9° shown in both samples belongs to the Al_2O_3 (0006). For the sample grown

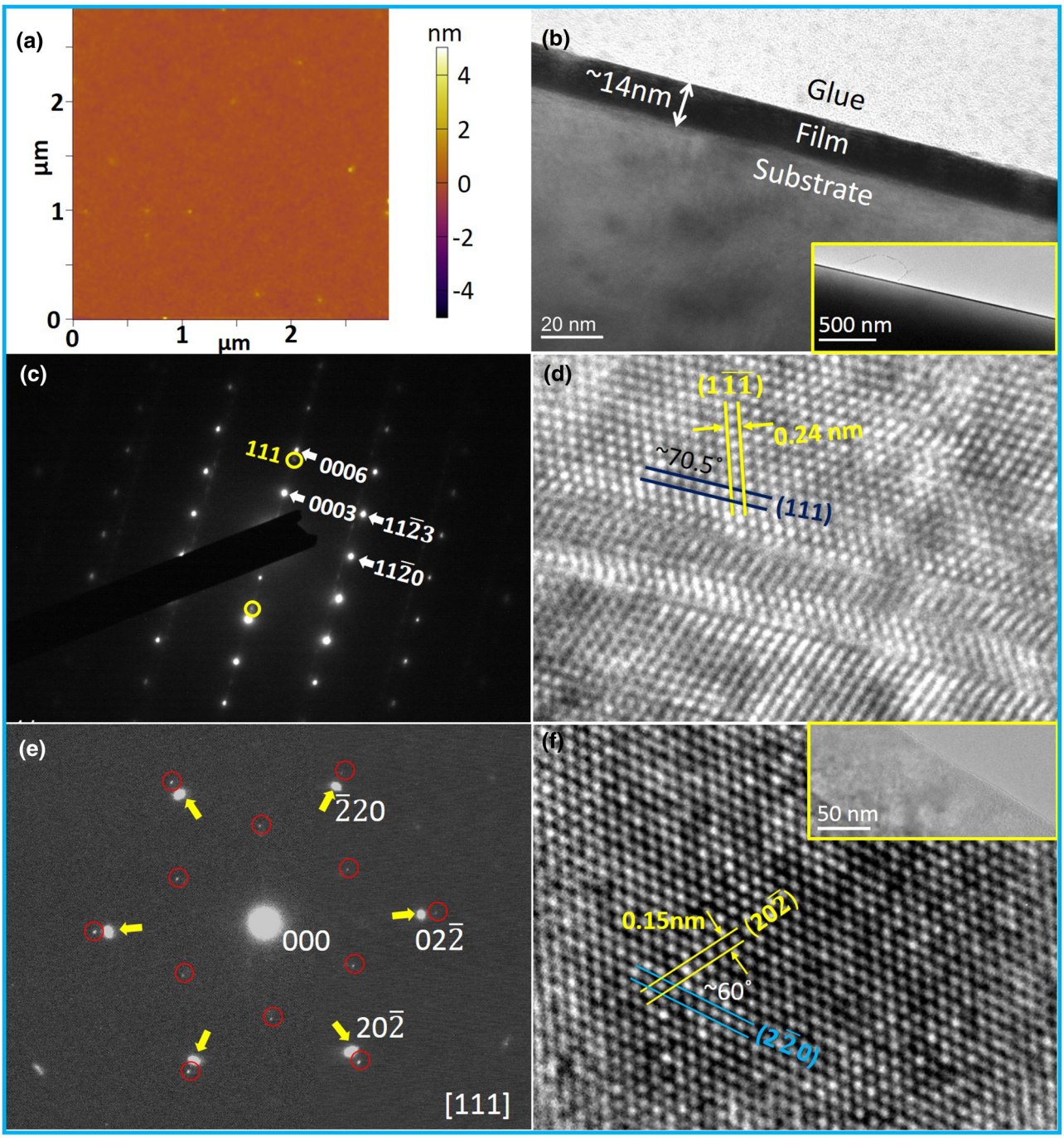

FIG. 2. AFM image and TEM investigations of Mo_2C film grown on the sapphire substrate. (a) AFM image showing the morphology of the as-grown Mo_2C thin film in large area. (b) Enlarged cross-sectional TEM image, and the inset shows a large area of Mo_2C film grown on the sapphire substrate. (c) The superimposed SAED pattern taken from both the film and substrate. The white arrowed spots belong to sapphire and the yellow circled spots belong to the film. (d) High-resolution TEM image taken from the cross section of the Mo_2C film. (e) SAED patterns taken from the overlapped area, including both the substrate and the grown film in the plane-view TEM sample. The yellow arrowed spots belong to the film and the red circled spots belong to the substrate. (f) High-resolution TEM image taken from the plane view of the Mo_2C film. The inset shows the low-magnified plane-view TEM image of the film and the substrate.

in CH_4 plasma, besides the substrate signal, there is a peak at around 37°, suggesting that the film grown is fcc structured Mo_2C with growth direction of [111] and lattice parameter of $a = 0.4155$ nm (standard identification card JCPDS 15-0457). From the sample grown in CH_4, no Mo_2C peak can be found, and the peak at 40.4° belongs to cubic-structured Mo (110) (standard identification card JCPDS 01-1205). The XRD results confirm the XPS analysis, supporting the conclusion that the sample grown in CH_4 plasma is Mo_2C, while Mo metal is deposited in nonionized CH_4. Besides the different results from both XPS and XRD measurements, for the sample grown in CH_4 gas without plasma enhancement we could not

find a superconductivity transition as observed in Mo_2C. (This is discussed in the following sections.)

The unsuccessful synthesis of Mo_2C in nonionized CH_4 gas confirms the crucial role of plasma enhancement. As previously reported, the major ions produced from dissociation of methane are C^+, $CH_x{}^+$, and $C_2H_y{}^+$, while H^+, H, and H_2 are also generated during the ionization process [29,38,39]. Based on this fact, two speculations are made about the plasma-enhanced deposition process. First, the methane plasma is more active than methane molecules, making Mo atoms more easily react with carbon and form Mo-C compound. Second, the existence of hydrogen ions and atoms may prevent the formation of a higher valence state of molybdenum in compounds such as MoO_3 or MoC.

The microscopic morphology of the film is examined by atomic force microscopy (AFM). The result shown in Fig. 2(a) shows a flat surface of the large-area film with a roughness of 0.3 nm (rms R_q). The energy-dispersive mapping (EDS) of molybdenum and carbon shows a homogeneous distribution of the two elements (EDS result is shown in Fig. S2 [37]). The uniformity of the film is also confirmed from the indentical reflectivity patterns of the XRR measurement at different spots of the film. (The result is illustrated in the Supplemental Material, Fig. S5 [37].) To study the structure and quality of the thin film in detail, we prepared a sample for further investigation by TEM. Figure 2(b) is an enlarged cross-sectional TEM image showing the continuous thin film with a flat surface, and the inset shows a low-magnified cross-sectional TEM image indicating the large-area thin film grown on the substrate. According to the cross-sectional TEM images, the film thickness is determined to be ~14 nm. (The film's growth condition is provided in Supplemental Material Table S1, [37].) Selected area electron diffraction (SAED) was used to determine the orientation relationship between the film and substrate, and Fig. 2(c) shows such a combined pattern taken from both the film and substrate. Using the diffraction spots of the substrate as reference, the indexing of the diffraction spots of the film can be determined. These diffraction patterns prove the epitaxial growth of film on the sapphire substrate with a film growth direction of [111]. Figure 2(d) is a high-resolution TEM image of the film, where it can be proven that the lattice spacing and angles are in good agreement with fcc structure, and the growth direction of the thin film is [111].

In order to further investigate the crystal structure of the film, we also prepared the plane-view TEM sample, where the ion-milling process can mill off the substrate and remains on the grown film only at the edge of the thin region. Figure 2(e) shows the combined pattern taken from both the substrate and film. Using the diffraction spots of the substrate as reference, an epitaxial orientation relationship between the Mo_2C film and sapphire substrate is determined to be $(111)_{Mo_2C}/(0001)_{Al_2O_3}$ and $[10\bar{1}]_{film}/[10\bar{1}0]_{substrate}$. The inset in Fig. 2(f) shows a plane-view bright-field TEM image in low magnification, where the edge region is the film and the inner region includes both the film and substrate. Figure 2(f) is a high-resolution TEM image taken from the film region, where one can see that the lattice spacing of the planes in the two directions and the angle between these two planes match the fcc Mo_2C structure with a lattice parameter of $a = 0.416$ nm.

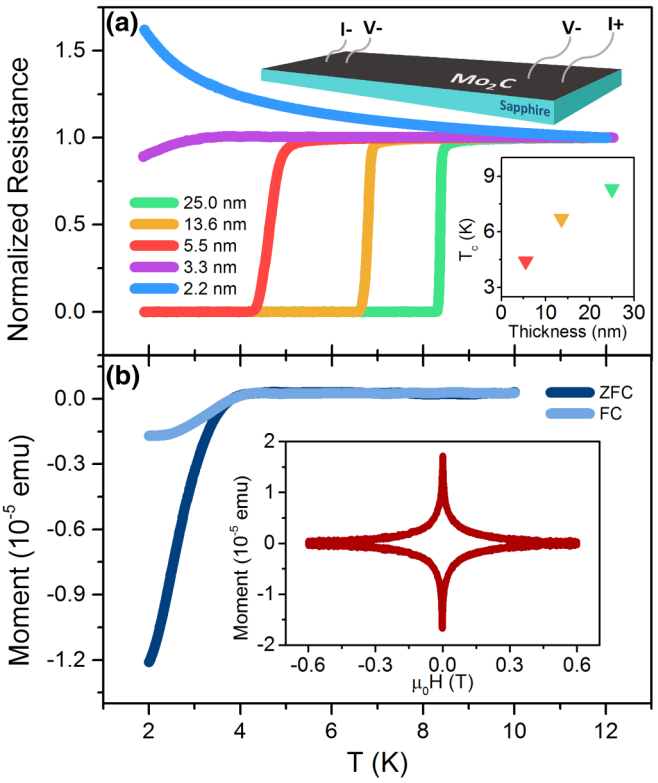

FIG. 3. Superconductivity transition of the Mo_2C films. (a) Thickness-dependent superconductivity of the Mo_2C film. Resistance change at temperatures from 2 K to 12 K is measured for samples with different thicknesses. The thickness is determined by XRR measurement. (XRR analysis is shown in the Supplemental Material Fig. S3, and their growth conditions are provided in the Supplemental Material, Table S1 [37].) The upper inset is a schema of the transport measurement configuration, while the lower inset is the relationship between the film thickness and its T_c. (b) Superconducting diamagnetic property of a 5.5-nm-thick sample. M-T is measured in ZFC and FC processes in a field of 10 Oe. The inset is the M-H loop from −0.6 to 0.6 T measured at 2 K.

We further studied the electrical transport properties of the grown thin films in the physical properties measurement system (PPMS). A schema of the four-probe resistance measurement configuration is illustrated as the upper inset in Fig. 3(a), in which Al wires are ultrasonically bonded on the sample surface as electrodes. Resistance is calculated as the ratio of the voltage across $V+$ and $V-$ over the constant current source of 0.5 μA through $I+$ and $I-$. The measurement of temperature-dependent resistance (R-T) on samples with different thicknesses is conducted, and the results show a thickness-dependent superconducting transition critical temperature (T_c). The critical transition temperature in this work is defined as the temperature where the resistance of the film drops to 10% of its resistance at normal state. We can see from the lower inset of Fig. 3(a) that the T_c decreases when the thickness of Mo_2C film is decreased until a critical thickness of 3.3 nm is reached, which does not turn to a superconducting state at 2 K. For the even thinner film with a thickness of 2.2 nm, the R-T curve turns out to be insulating. This result is consistent with previously reported superconductivity in molybdenum carbide films of different

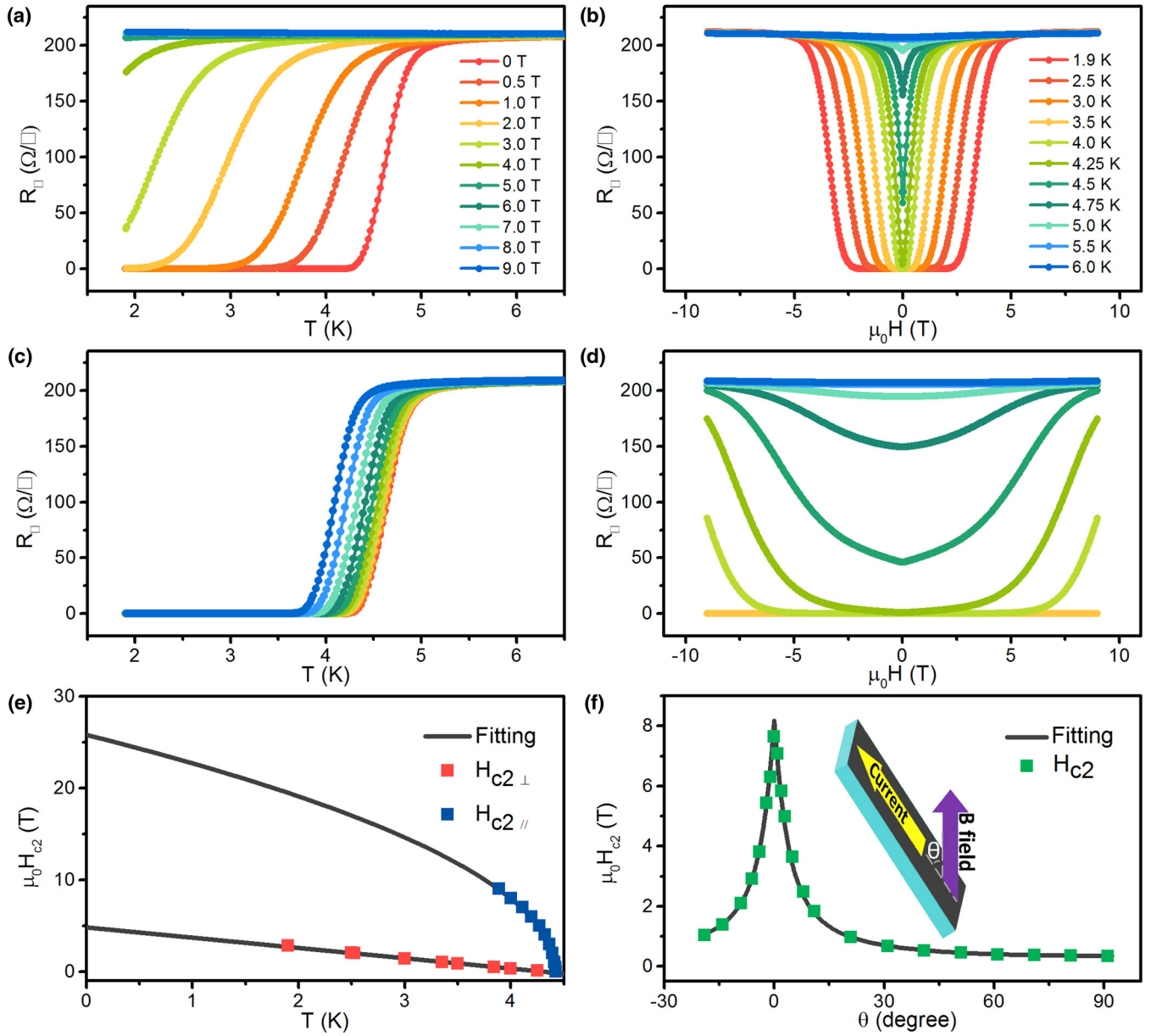

FIG. 4. The 2D superconductivity in a 5.5-nm Mo_2C film. (a) Temperature dependence of resistivity under an out-of-plane magnetic field of different strengths. (b) Magnetoresistance under an out-of-plane magnetic field at different temperatures. (c) Temperature-dependent resistivity under an in-plane magnetic field of different strengths. The color code is the same as that in Fig. 4(a). (d) Magnetoresistance under an in-plane magnetic field at different temperatures. The color code is the same as that in Fig. 4(b). (e) The temperature-dependent H_{c2} analysis and the 2D GL theory fitting. The H_{c2} is defined as the field where the resistance drops to 10% of the normal resistance. (f) The relationship of the H_{c2} and the angle θ between the magnetic field relative and the current direction, which is illustrated in the inset.

cyrstal structures [9,24,28], showing a higher T_c for thicker films. The phenomenon that T_c increases in thicker samples was not only observed in Mo_2C, but also in other materials like Bi, Nb, and $NbSe_2$ [40–42], where the 2D superconductivity was illustrated. Such thickness dependence is predicted by the Cooper law [43], which is commonly used to fit the thickness-dependent superconducting temperature T_d of film with its thickness d thinner than the superconducting coherent length:

$$T_d = T_{c0} e^{(-2a/N_0 V d)},$$

where a is the nonsuperconducting surface layer thickness on each side of the film, T_{c0} is the bulk critical temperature, and N_0V is the bulk interaction potential. The suppression of T_c in thinner films can result from the decrease of the density of states near the surface, which is obtained from a proximity effect model. Further work is needed to investigate the underlying physical mechanism that contributes to the reduction of T_c in thinner Mo_2C films, while the superconducting order parameter change along the out-of-plane direction, the penetration effect, and quantum size effect might shed light on the problem.

The temperature dependence of magnetization (M-T) under an out-of-plane magnetic field of 10 Oe was measured after zero-field-cooling (ZFC) and field-cooling (FC) processes. As shown in Fig. 3(b), the M-T curves exhibit a drop

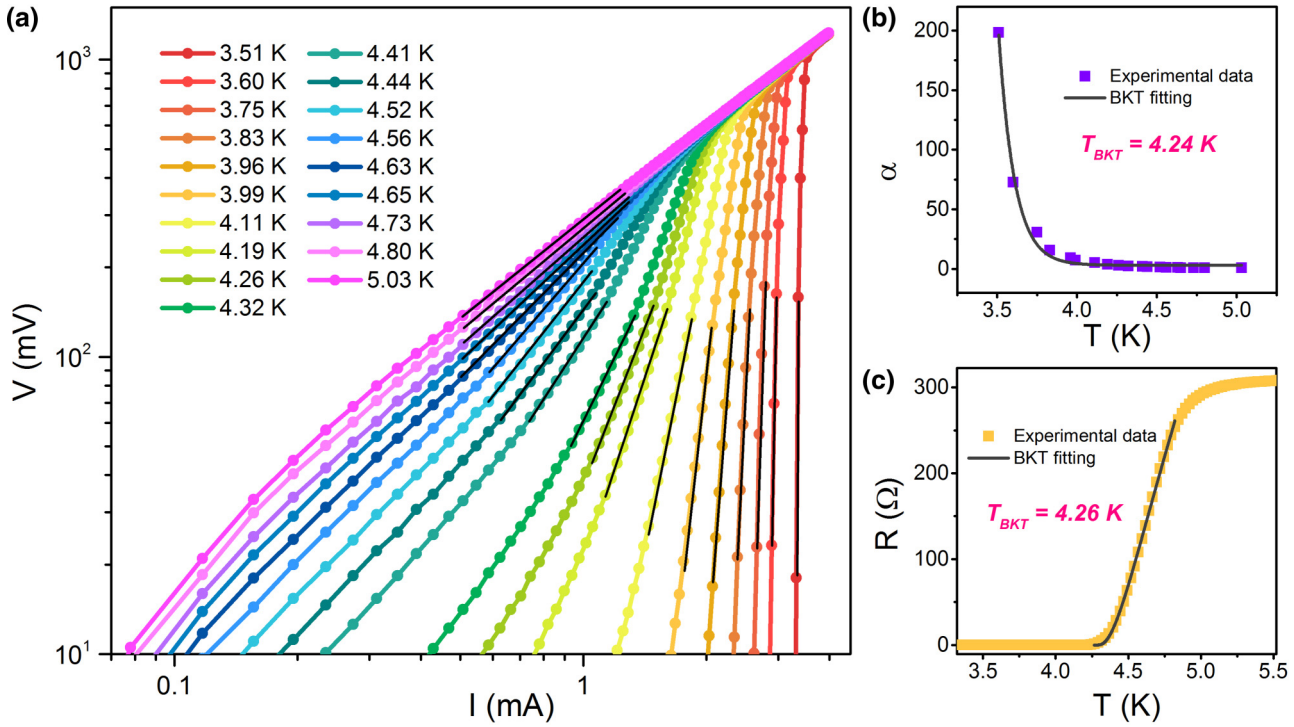

FIG. 5. V-I measurement for the a 5.5-nm Mo_2C film and its BKT transition. (a) V-I curves in logarithm scale. The black lines are fittings of the data in the transition, and its slope is abstracted as α. (b) The temperature dependence of the power-law exponent α, which is extracted from Fig. 5(a). The fitting for a BKT transition is 4.24 K. (c) The R-T fitting for a BKT transition with $T_{\mathrm{BKT}} = 4.26$ K.

crossover at around 4 K, indicating a diamagnetic response below the critical temperature, and confirms the occurrence of superconductivity. The relationship between field strength and magnetization (M-H loop) measured at 2 K, shown in the inset of Fig. 3(b), exhibits clear magnetic hysteresis. This indicates that Mo_2C is a typical type-II superconductor.

For the electrical transport measurements, we systematically investigated the much thinner sample, a 5.5-nm-thick film, to study its two-dimensional superconductivity, which is expected to exist in sufficiently thin samples. The influence of external magnetic field on the superconducting characteristics of a 5.5-nm-thick Mo_2C film is shown in Figs. 4(a)–4(d), the magnetic fields are out-of-plane and in-plane, respectively. One can see that T_c turns out to be lower when a magnetic field is applied to the film, revealing an obvious suppression of the superconductivity. It is also apparent that the response to magnetic field is anisotropic in this system. We determine the upper critical magnetic field H_{c2} as the one where the resistance drops to 10% of the normal resistance. The temperature-dependent H_{c2} under both field orientations are extracted from Figs. 4(a)–4(d) and plotted in Fig. 4(e). As described by the Ginzburg-Landau (GL) theory of 2D superconductors [44], coherence length and effective thickness can be further derived from $Hc_{2\parallel}$ (T) and $Hc_{2\perp}$ (T) with the following relations:

$$H_{c2,\perp} = \frac{\Phi_0\sqrt{12}}{2\pi\xi_{GL}^2(0)}\left(1-\frac{T}{T_c}\right),$$

$$H_{c2,\parallel} = \frac{\Phi_0\sqrt{12}}{2\pi\xi_{GL}(0)d_{SC}}\left(1-\frac{T}{T_c}\right)^{\frac{1}{2}},$$

where $\xi_{GL}(0)$ is the zero-temperature GL in-plane coherence, Φ_0 is the magnetic flux quantum, and d_{SC} is the out-of-plane superconducting effective thickness. From the fitting, the coherent length is determined to be 8.3 nm. An effective thickness of 5.3 nm is obtained, which is consistent with the XRR result of 5.5 nm (Supplemental Material, Fig. S3 [37]). It is also noted that the H_{c2} (0 K) in the parallel magnetic field is as large as 25.8 T and in the perpendicular field it is 4.8 T, which is much larger than those of the ultrathin α-Mo_2C phase [9,10,28]. The enhanced superconductivity from our fcc-Mo_2C film with higher T_c and H_{c2} may be related to the difference of crystal structure, film growth direction, and structural defects induced by variant growth methods. Another tool to verify the 2D superconductivity of the sample is the Tinkham formula,

$$\left|\frac{H_{c2}(\theta)\sin\theta}{H_{c2,\perp}}\right| + \left(\frac{H_{c2}(\theta)\cos\theta}{H_{c2,\parallel}}\right)^2 = 1,$$

which describes the relationship between the upper critical field H_{c2} and the angle θ of the magnetic field relative to the current direction. In considering the large H_{c2} at lower temperatures, the angle dependence of the upper critical field at 4 K was investigated. Magnetoresistance under fields of various directions is measured (Supplemental Material, Fig. S4 [37]), from which the H_{c2} under different field directions is extracted. The $H_{c2}(\theta)$ and the well-fitted curve from the Tinkham formula are plotted in Fig. 4(f). This result further proves the 2D superconductivity in the Mo_2C film.

The voltage-current (V-I) characteristics of this system were also measured at selected temperatures without the

presence of an external magnetic field. The results are shown in Fig. 5(a), where the V-I curves under temperatures of 3.51–5.03 K are illustrated. As predicted by the BKT model, the V-I curves follow a $V \propto I^{\alpha}$ power-law dependence, which can be seen from the linear fitting lines in the log-log scale [45–47]. The temperature dependence of α is shown in Fig. 5(b), where the BKT transition temperature (T_{BKT}) is determined as 4.24 K when α reaches 3. This value is almost the same as the onset temperature when zero resistance appears. Meanwhile, the R-T characteristic can also be fitted by the BKT formula,

$$R = R_0 \exp\left[-b\left(\frac{T}{T_{\mathrm{BKT}}} - 1\right)^{1/2}\right],$$

where R_0 and b depend on material only. As shown in Fig. 5(c), the fitting analysis gives $T_{\mathrm{BKT}} = 4.26$ K, which is highly consistent with the V-I results. The analysis on the V-I characteristics reveals the signature of BKT transition, which is another evidence for its 2D superconductivity.

IV. CONCLUSION

In summary, single-crystalline Mo_2C thin films have been epitaxially grown by a plasma-enhanced pulsed-laser deposition method, where the ionized CH_4 gas plays a crucial role in the synthesis process. The grown single-crystalline Mo_2C has the largest area reported so far, and it has a rarely reported fcc structure. Consistent with the Berezinskii-Kosterlitz-Thouless transition model, their electric and magnetic properties show a typical two-dimensional superconductivity. The PEPLD method introduced here can also be applied in other large-area TMC synthesis methods, offering researchers an important reference for further study on the TMCs, particularly their applications.

ACKNOWLEDGMENTS

This work was supported by the NSFC/RGC through Grant No. N-PolyU517/14, the Postdoctoral Fellowships Scheme of the Hong Kong Polytechnic University through Projects No. G-YW0A and No. 1-YW0T, and The Hong Kong Polytechnic University Strategic Importance through Project No. 1-ZE25.

F.Z., Z.Z., and H.W. contributed equally to this work.

[1] S. Z. Butler, S. M. Hollen, L. Cao, Y. Cui, J. A. Gupta, H. R. Gutiérrez, T. F. Heinz, S. S. Hong, J. Huang, A. F. Ismach, E. Johnston-Halperin, M. Kuno, V. V. Plashnitsa, R. D. Robinson, R. S. Ruoff, S. Salahuddin, J. Shan, L. Shi, M. G. Spencer, M. Terrones, W. Windl, and J. E. Goldberger, ACS Nano **7**, 2898 (2013).

[2] K. S. Novoselov, A. Mishchenko, A. Carvalho, and A. H. Castro Neto, Science **353**, aac9439 (2016).

[3] D. Deng, K. S. Novoselov, Q. Fu, N. Zheng, Z. Tian, and X. Bao, Nat. Nano **11**, 218 (2016).

[4] V. Nicolosi, M. Chhowalla, M. G. Kanatzidis, M. S. Strano, and J. N. Coleman, Science **340**, 1226419 (2013).

[5] M. Naguib, O. Mashtalir, J. Carle, V. Presser, J. Lu, L. Hultman, Y. Gogotsi, and M. W. Barsoum, ACS Nano **6**, 1322 (2012).

[6] M. Naguib, M. Kurtoglu, V. Presser, J. Lu, J. Niu, M. Heon, L. Hultman, Y. Gogotsi, and M. W. Barsoum, Adv. Mater. **23**, 4248 (2011).

[7] M. Naguib, V. N. Mochalin, M. W. Barsoum, and Y. Gogotsi, Adv. Mater. **26**, 992 (2014).

[8] M. Khazaei, M. Arai, T. Sasaki, C.-Y. Chung, N. S. Venkataramanan, M. Estili, Y. Sakka, and Y. Kawazoe, Adv. Funct. Mater. **23**, 2185 (2013).

[9] C. Xu, L. Wang, Z. Liu, L. Chen, J. Guo, N. Kang, X.-L. Ma, H.-M. Cheng, and W. Ren, Nat. Mater. **14**, 1135 (2015).

[10] L. Wang, C. Xu, Z. Liu, L. Chen, X. Ma, H.-M. Cheng, W. Ren, and N. Kang, ACS Nano **10**, 4504 (2016).

[11] M. W. Barsoum and M. Radovic, Annu. Rev. Mater. Res. **41**, 195 (2011).

[12] M. T. Agne, M. Radovic, G. W. Bentzel, and M. W. Barsoum, J. Alloys Compd. **666**, 279 (2016).

[13] K. Hantanasirisakul, M.-Q. Zhao, P. Urbankowski, J. Halim, B. Anasori, S. Kota, C. E. Ren, M. W. Barsoum, and Y. Gogotsi, Adv. Electron. Mater. **2**, 1600050 (2016).

[14] M. Ghidiu, M. R. Lukatskaya, M.-Q. Zhao, Y. Gogotsi, and M. W. Barsoum, Nature **516**, 78 (2014).

[15] M. R. Lukatskaya, O. Mashtalir, C. E. Ren, Y. Dall'Agnese, P. Rozier, P. L. Taberna, M. Naguib, P. Simon, M. W. Barsoum, and Y. Gogotsi, Science **341**, 1502 (2013).

[16] M. Naguib, J. Halim, J. Lu, K. M. Cook, L. Hultman, Y. Gogotsi, and M. W. Barsoum, J. Am. Chem. Soc. **135**, 15966 (2013).

[17] B. Xu, M. Zhu, W. Zhang, X. Zhen, Z. Pei, Q. Xue, C. Zhi, and P. Shi, Adv. Mater. **28**, 3411 (2016).

[18] X. H. Wang and Y. C. Zhou, J. Mater. Sci. Technol. **26**, 385 (2010).

[19] Y. Wang, F. Li, Y. Li, and Z. Chen, Nat. Commun. **7**, 11488 (2016).

[20] R. H. Willens, E. Buehler, and B. T. Matthias, Phys. Rev. **159**, 327 (1967).

[21] M. Wu, X. Lin, A. Hagfeldt, and T. Ma, Angew. Chem. Int. Ed. **50**, 3520 (2011).

[22] C. Wan, Y. N. Regmi, and B. M. Leonard, Angew. Chem. Int. Ed. **53**, 6407 (2014).

[23] H. Vrubel and X. Hu, Angew. Chem. Int. Ed. **51**, 12703 (2012).

[24] S. J. Lee and J. B. Ketterson, Phys. Rev. Lett. **64**, 3078 (1990).

[25] T. P. St. Clair, S. T. Oyama, D. F. Cox, S. Otani, Y. Ishizawa, R.-L. Lo, K.-i. Fukui, and Y. Iwasawa, Surf. Sci. **426**, 187 (1999).

[26] C. A. Wolden, A. Pickerell, T. Gawai, S. Parks, J. Hensley, and J. D. Way, ACS Appl. Mater. Interfaces **3**, 517 (2011).

[27] J. Halim, S. Kota, M. R. Lukatskaya, M. Naguib, M.-Q. Zhao, E. J. Moon, J. Pitock, J. Nanda, S. J. May, Y. Gogotsi, and M. W. Barsoum, Adv. Funct. Mater. **26**, 3118 (2016).

[28] D. Geng, X. Zhao, L. Li, P. Song, B. Tian, W. Liu, J. Chen, D. Shi, M. Lin, W. Zhou, and K. P. Loh, 2D Mater. **4**, 011012 (2017).

[29] M. Meyyappan, D. Lance, C. Alan, and H. David, Plasma Sources Sci. Technol. **12**, 205 (2003).
[30] D. A. Boyd, W. H. Lin, C. C. Hsu, M. L. Teague, C. C. Chen, Y. Y. Lo, W. Y. Chan, W. B. Su, T. C. Cheng, C. S. Chang, C. I. Wu, and N. C. Yeh, Nat. Commun. **6**, 6620 (2015).
[31] A. Dato, V. Radmilovic, Z. Lee, J. Phillips, and M. Frenklach, Nano Lett. **8**, 2012 (2008).
[32] A. Ohtomo and H. Y. Hwang, Nature (London) **427**, 423 (2004).
[33] J. Bohandy, B. F. Kim, and F. J. Adrian, J. Appl. Phys. **60**, 1538 (1986).
[34] S. R. Sarath Kumar and H. N. Alshareef, Appl. Phys. Lett. **102**, 012110 (2013).
[35] D. J. Late, P. A. Shaikh, R. Khare, R. V. Kashid, M. Chaudhary, M. A. More, and S. B. Ogale, ACS Appl. Mater. Interfaces **6**, 15881 (2014).
[36] Z. Yang, J. Hao, S. Yuan, S. Lin, H. M. Yau, J. Dai, and S. P. Lau, Adv. Mater. **27**, 3748 (2015).
[37] See Supplemental Material at http://link.aps.org/supplemental/10.1103/PhysRevMaterials.1.034002 for the illustration of the plasma-enhanced pulsed-laser deposition system, the dimension and EDS mapping of the Mo_2C ultrathin film grown on sapphire, the XRR analysis of sample thickness ranging from 3.3 to 25 nm, magnetoresistance under field of variant directions, and the thickness of samples grown for different times.
[38] M. J. Vasile and G. Smolinsky, Int. J. Mass Spectrom. Ion Phys. **18**, 179 (1975).
[39] K. Hiraoka, K. Aoyama, and K. Morise, Can. J. Chem. **63**, 2899 (1985).
[40] D. B. Haviland, Y. Liu, and A. M. Goldman, Phys. Rev. Lett. **62**, 2180 (1989).
[41] M. S. M. Minhaj, S. Meepagala, J. T. Chen, and L. E. Wenger, Phys. Rev. B **49**, 15235 (1994).
[42] X. Xi, Z. Wang, W. Zhao, J.-H. Park, K. T. Law, H. Berger, L. Forro, J. Shan, and K. F. Mak, Nat. Phys. **12**, 139 (2016).
[43] L. N. Cooper, Phys. Rev. Lett. **6**, 689 (1961).
[44] M. Tinkham, *Introduction to Superconductivity*, 2nd ed. (Dover Publications, Inc., Mineola, New York, 2004).
[45] V. L. Berezinskii, Zh. Eksp. Teor. Fiz. **61**, 1144 (1972) [Sov. Phys. JETP **34**, 610 (1972)].
[46] J. M. Kosterlitz and D. J. Thouless, J. Phys. C: Solid State Phys. **5**, L124 (1972).
[47] N. Reyren, S. Thiel, A. D. Caviglia, L. F. Kourkoutis, G. Hammerl, C. Richter, C. W. Schneider, T. Kopp, A.-S. Rüetschi, D. Jaccard, M. Gabay, D. A. Muller, J.-M. Triscone, and J. Mannhart, Science **317**, 1196 (2007).